Damage and fracture studies of continuous flax fiber-reinforced composites 3D printed by in-nozzle impregnation additive manufacturing

Xikun Wu, Geoffrey Ginoux, joseph paux, Samir Allaoui

Special Issue: Damage Behavior of Bio Composites

INTERNATIONAL JOURNAL OF DAMAGE MECHANICS

International Journal of Damage Mechanics
0(0) 1–22

DOI: 10.1177/10567895241279845
journals.sagepub.com/home/ijd
Sage

Damage and fracture studies of continuous flax fiber-reinforced composites 3D printed by in-nozzle impregnation additive manufacturing

Xikun Wu, Geoffrey Ginoux, Joseph Paux and Samir Allaoui

Abstract

Additive manufacturing (AM) of continuous yarn-reinforced biobased composites presents multi-functional properties and low environmental impact of this technology. Few studies focused on the mechanical damage mechanisms of continuous biobased composites obtained by AM processes, while it is a topic of high interest for the mastery of mechanical behaviors and optimization of the materials for high requirement applications. This study aims to assess the damage and fracture modes of continuous flax yarn-reinforced PLA manufactured by AM, with different yarn orientations. The additively manufactured biobased composites were characterized by tensile test, 3D microscopy and micro-tomography to link the process-structure-properties relationships regarding the damage and fracture modes. The results showed that the 0° manufactured composite had a significant enhancement of tensile properties compared to other configurations. The damage mechanism presented fiber rupture with polymer transverse cracks at 0°, while the 45° and 90°-oriented composites showed premature fiber/matrix interface debonding. This study aims to find the relationship between damage mechanisms, deposition strategy, and anisotropy of the additively manufactured long vegetal fibers-reinforced biobased composite materials. The results bring a new understanding of the anisotropy and defects in printed composite materials regarding their mechanical behaviors during damage.

Keywords

In-nozzle impregnation additive manufacturing, continuous biobased composite, tensile properties, mechanical damage, microscope, tomography

Institut de Thermique, Mécanique, Matériaux (EA 7548), MATUR Chair, University of Reims Champagne-Ardenne, EiSINe, Charleville-Mézières, France

Corresponding author:
Samir Allaoui, Université de Reims Champagne-Ardenne, 9A Rue Claude Chretien, Charleville Mézières 08000, France.
Email: samir.allaoui@univ-reims.fr

Introduction

In recent years, additive manufacturing (AM), also known as 3D printing, has become a significant technology applied in both industrial and academic fields. Compared to conventional manufacturing technologies, AM has faster fabrication speed for small production series, lower cost and less environmental impact, and brings freedom in design choice (Pereira et al., 2019). Its applications range from high specific performance to multi-functional materials with complex geometries. Among all types of AM processes, the Fused Filament Fabrication (FFF) is the most used one. The FFF uses a filament feedstock and manufactures parts by depositing molten polymer rasters, layer by layer, on a build plate. However, parts manufactured by FFF with polymeric materials require the use of composite materials to increase their mechanical performances. The addition of nano- or micro-reinforcement is easy to implement but tends to increase the rigidity to the detriment of the ultimate tensile strength (UTS) or elongation at break (Balla et al., 2019; Ginoux et al., 2021). One way to overcome this issue is the AM of continuous or long fiber composite materials that exhibit superior mechanical performance compared to short fiber-charged composite (Isobe et al., 2018) and similar mechanical behaviors as traditional orthotropic unidirectional composites (Dutra et al., 2020), as all the fibers are oriented along one direction continuously throughout the whole material so that it provides the material with higher mechanical resistance along the fiber orientation.

Two main methods exist to additively manufacture continuous fiber-reinforced materials (J. Zhang et al., 2020). The first method uses a single reinforced composite filament where the yarn was coated or impregnated before printing (Sugiyama et al., 2020). The second method combines a continuous yarn/roving and a molten thermoplastic filament inside the printing nozzle and extrudes them out as a continuous printing raster, which is known as in-nozzle impregnation composite AM or real-time in-situ AM (Kasmi et al., 2021; Kuschmitz et al., 2021; Terekhina et al., 2022). Whatever the method, the composite AM process applies less pressure than conventional composite manufacturing methods, which potentially induces a weaker impregnation effect and weak fiber/matrix interface bonding. This was highlighted by Khosravani et al. (2022b), who found that the increase of the continuous glass fiber content leads to an extensive fiber breakage at the fracture area, which indicated that the fiber took more dominance in the composite tensile loading and that the increase of fiber content to some degree could potentially increase the inter-fiber voids and weaken the interfacial properties. The absence of high pressure in AM also causes porosity inside the specimens, weakening the AM materials' mechanical properties (Rao et al., 2021). In addition, the polymer/polymer interface inherent to the raster-by-raster and layer-by-layer process for AM is subject to inter-raster and inter-layer delamination during mechanical solicitations, as was shown with carbon fiber-reinforced polymer and glass fiber-reinforced polymer obtained by Heitkamp et al. (2023). Therefore, additive processes inherently induce structures or different qualities of the printed materials, which will impact its behavior and specifically that at breakage. So, the mastery of the AM process for composite materials and the induced behavior and damage mechanisms is an important issue.

The continuous fiber reinforcements for AM are classified in two categories: synthetic fibers such as carbon fiber (van de Werken et al., 2020) and glass fiber (Chen et al., 2021; Saidane et al., 2022); and natural fibers such as flax fiber (Kuschmitz et al., 2021; Le Duigou et al., 2019; Terekhina et al., 2022), jute fiber (Matsuzaki et al., 2016) and ramie fiber (Cheng et al., 2021). Synthetic fibers tend to have higher mechanical performance than natural fibers such as tensile strength and elastic modulus, but natural fibers have high damping properties (Liu et al., 2021) and better performances in acoustic and thermal insulation (Bahrami et al., 2020) and substantially lower cost than synthetic

fibers, which gives natural fibers higher performance price ratio (modulus/cost) (Bisanda and Ansell, 1992; A. Mohanty et al., 2000; Ramamoorthy et al., 2015). Therefore, natural fiber-reinforced composites have a strong application potential linked to their specific properties. In this context, studies on the additively manufactured continuous natural fiber-reinforced composites have been carried out by researchers in recent years. Matsuzaki et al. (2016) have found that the additively manufactured continuous jute yarns (volume fraction = 6.1%) reinforced PLA by in-nozzle impregnation has brought enhancement on tensile modulus and strength by 157% and 134%, respectively, while Kuschmitz et al. (2021) have found that the continuous flax yarns (volume fraction = 24.54%) reinforced PLA by in-nozzle impregnation AM had tensile modulus and strength increased by 3.55 and 2.25 times compared to the pure PLA, which is mainly due to the higher reinforcement content. Le Duigou et al. (2019) have additively manufactured composites by using a single continuous flax yarn-reinforced PLA filament with optimized layer height. The results showed that the obtained AM composite with flax volume fraction of 30.4% had mechanical properties as good as certain carbon and glass fiber-reinforced composites by AM. They also found clean fiber pull-out and fiber/matrix debonding at fracture surface. These effects were mainly due to the imperfect impregnation caused by the nature of the yarn itself and its highly twisted fiber bundle structure, same damage phenomenon of 3D printed continuous composite were also found in the study of (H. Zhang and Sun, 2022) for continuous basalt fiber and (Mohammadizadeh and Fidan, 2021) for continuous carbon fiber.

Still, the mechanical behavior of continuously reinforced composites by AM with plant fiber reinforcements is not yet fully understood, especially regarding their damage mechanisms, which are strongly influenced by their internal structures compared to carbon and glass fibers. The current state of the art lacks characterizations with standardized method to avoid edge effects, as pointed out in Ginoux et al. (2023), which affects the quality of the samples and the induced behavior, and therefore the damage mechanisms. Different loadings – not only for 0° tensile tests – are also required to enhance the mastery of the anisotropy of the material.

This study aims to evaluate the quality and properties of continuous reinforced biobased composites by AM and their mechanical behavior and associated damage mechanisms thanks to an adapted preparation of the specimens for the characterization regarding the anisotropy. For this, continuous flax/PLA composites were manufactured by in-nozzle impregnation AM at different raster orientations and tested mechanically by tensile tests to study the damage phenomena of the continuous biobased composites 3D printed by in-nozzle impregnation AM. X-ray micro-computed tomography (X-μCT) and 3D microscopy were used to observe and analyze the internal structure and surface damages after tensile test of the composites and link them with the mechanical behaviors. The relation between composite structures, properties, and damage phenomena was drawn for a better understanding and mastery of this technology.

Materials and methods

Materials

The manufacturing of the composite materials was carried out with a flax yarn and a commercially available polymer filament. The flax yarn used in this study was purchased from FRD (France) under the reference Y32. Table 1 displays the physical properties of the yarn. The thermoplastic filament is supplied by Nanovia (France) under the reference PLA EF 3D850 in its native color. The physical properties of the polymer filament are shown in Table 2.

Table 1. Physical properties of the Y32 flax yarn from supplier.

Physical properties	Flax fiber yarn
Diameter (mm)	0.35
Linear mass (Tex)	105
Twist per meter (tpm)	150
Density (g/cm^3)	1.3

Table 2. Physical properties of the PLA EF 3D850 filament from supplier.

Physical properties	PLA filament
Diameter (mm)	1.75
Density (g/cm^3)	1.24
Young's modulus (MPa)	3540
Ultimate tensile strength (MPa)	58
Elongation at break (%)	2.6
Izod impact (kJ/m^2)	1.18
Glass transition temperature (°C)	55–60
Melt flow rate (g/min)	7–9

Specimen preparation method

Continuous fiber biobased composite plates were manufactured by in-nozzle impregnation AM with a Composer A4 3D printer from Anisoprint (Russia). One flax yarn and two neat PLA filaments – one for printing pure polymer layers, another for in-nozzle impregnation with the flax yarn to print composite layers – were used (see Figure 1). $250 \times 120 \times 2.30\,\text{mm}^3$ biobased composite plates were printed with different raster orientations, namely 0°, 45° and 90° compared to the length of the plate. Fixed printing settings are displayed in Table 3. The layer composition and stacking sequence of the plate are exhibited in Figure 2. A thin layer of micro-infill was used for better adhesion with the build plate. The second and last polymer layers were added for consolidation and part quality.

After manufacturing of the flax/PLA composite plate, specimens were machined from each plate. Dimensions were adapted from the ASTM D 3039 standard for tensile testing of composite materials (see Figure 3). According to the study of Ginoux et al. (2023), this hybrid additive/subtractive preparation avoids the edge effects and the microstructure variabilities from flow deposition irregularities and thermal history variation, which avoids, among other things, the over-estimation of the mechanical properties of the 90° specimens. Six specimens were cut from each plate (as shown in Figure 4) with a TS 55 FEBQ rotative steel plate saw from Festool (Germany). The 0° plate and 90° plate were cut into six tensile specimens per plate while the 45° plates were cut into three tensile specimens per plate in the middle to avoid difference in thermal history brought by the areas with short AM trajectories (shown in blue triangles) compared to 0° and 90° specimens.

Material characterization

The tensile tests of the AM specimens were performed on a universal testing machine Instron 3366 (USA) with a 10 kN load cell and equipped with a video extensometer. Tests were performed at a 2 mm/min crosshead speed at room temperature of 20°C. The video extensometer was used to

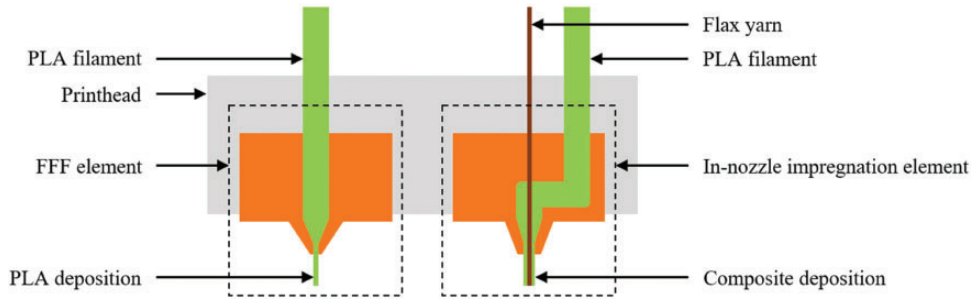

Figure 1. Filament extrusion and AM system from Anisoprint Composer A4.

Table 3. Printing parameters and associated values for the AM of continuous fiber biobased composite plates.

Parameters	Values
Printing speed	60 mm/s
Nozzle temperatures	205°C
Build plate temperature	60°C
Nozzle diameter for pure polymer	0.4 mm
Nozzle diameter for composite	0.8 mm
Layer height	0.35 mm
Extrusion coefficient	1.2

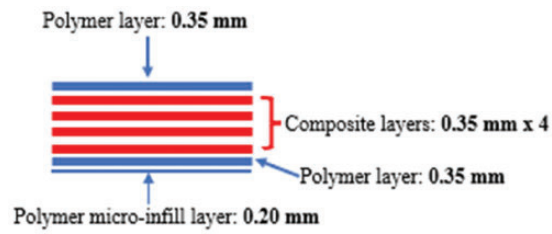

Figure 2. Layer composition and stacking sequence of the composite plates printed by in-nozzle impregnation.

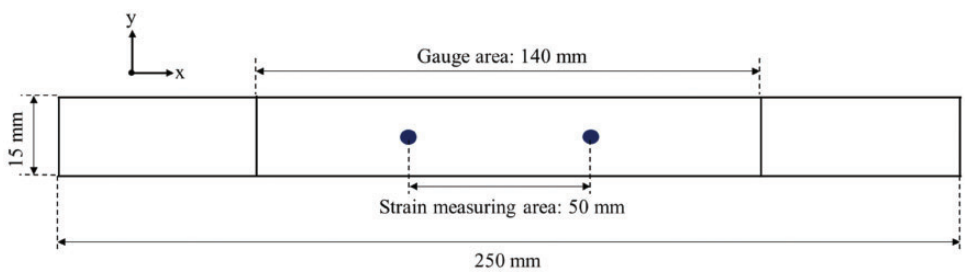

Figure 3. ASTM D 3039 tensile specimen standard.

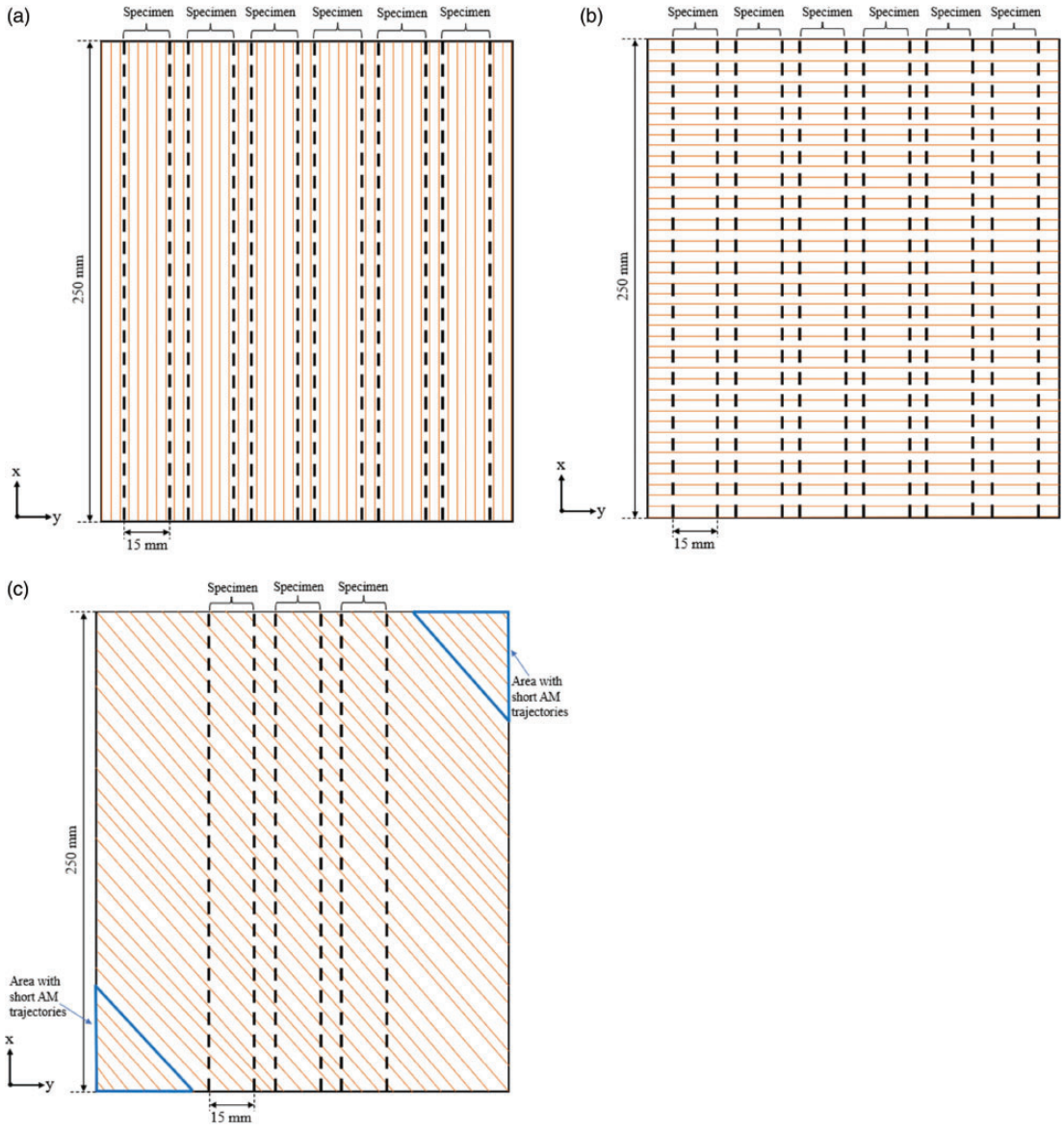

Figure 4. Schema of the specimens cutting method from the AM composite plates at 0° (a), 90° (b), and 45° (c).

measure the sample strains during tensile test with the help of two dark blue marks of 5 mm in diameter separated by a 50 mm distance and centered in the middle of the gauge section surface (see Figure 3). All samples were measured in thickness and width three times with an ABS Digimatic electronic caliper from Mitutoyo (Japan) with a 0.01 mm precision to calculate the section of each specimen. All the specimens were dried at 45°C for 16 h before the tensile test to remove the moisture absorbed from the environment by the PLA/flax composites, which could avoid the impact of moisture on tensile properties of the biobased composites (Dhakal et al., 2007). For each material configurations, six specimens were tested for statistical analysis.

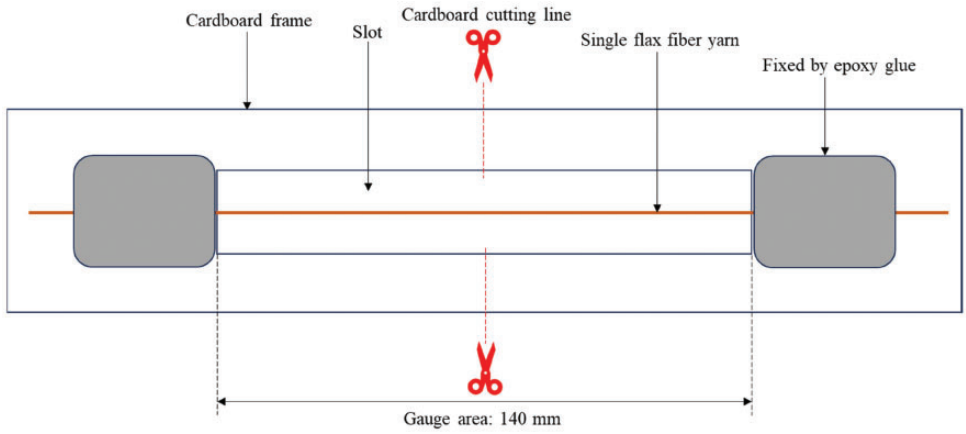

Figure 5. ASTM C 1557 single fiber tensile test standard.

To evaluate the consistency of the measured properties of the printed composites, mechanical characterizations were performed on its constituents i.e., the flax yarn and the polymer. Tensile tests were done on the flax yarns drawing inspiration from the ASTM C 1557 standard relating to the tensile characterization of fibers. This protocol with the same conditions has already been successfully adapted for flax yarns (Moothoo et al., 2014). The same Instron 3366 machine at the same environmental condition but with a 100 N load cell and a 1 mm/min crosshead speed. The flax yarn was fixed on a cardboard frame with a Loctite EA3479A/B epoxy glue from Henkel (Germany) to avoid fiber distortion and damage during the handling (see Figure 5). The cardboard frame was cut from the middle when the sample was successfully mounted on the test machine before launching the tensile test. The crosshead displacement is used to calculate the yarn's displacement according to the ASTM C 1557 standard by correcting with the system compliance of the used apparatus, $C_S = 1.498{\cdot}10^{-7}$ m/N, (see equation (1)).

$$\Delta l = \Delta L - C_S \times F \tag{1}$$

With Δl the displacement of the yarn gauge section, ΔL the recorded displacement of the crosshead and, F the measured force at the associated displacement of the crosshead.

We note that the coefficient C_S is quite low, which implies that the effect of compliance will be weak for low efforts. This is why the displacement of the cross head is often used by the scientific community working on fibrous media to measure the yarn deformation, like biobased (Moothoo et al., 2014) or commingled ones (Rocher et al., 2015), given the inadequacy of using classical techniques such as the DIC or extensometer, etc.

The cross-sectional area of the flax yarn was measured by tomographic observation. The characterization of the polymer mechanical behavior was performed on specimens, according to the type 1B from ISO 527-2 standard (shown in Figure 6), printed with the same conditions as the biobased composite (See Table 3). The only difference is the nozzle diameter and layer height which are 0.4 mm and 0.2 mm respectively. The PLA 0° AM specimens are printed so that the print direction (print nozzle travel direction) faces the tensile test direction. The characterization of the printed polymer without fiber reinforcements makes it possible to have the characteristics considering the

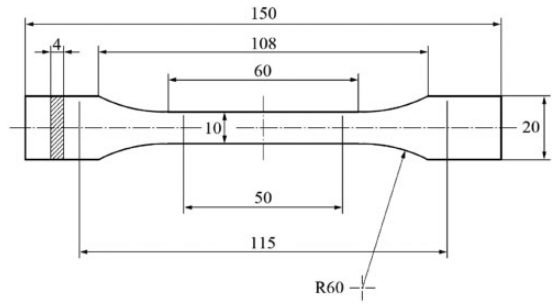

Figure 6. Type 1B tensile test specimen according to ISO 527-2 standard. Dimensions are expressed in millimeter.

effect induced by the printing process. Six specimens were tested with the same universal testing machine and parameters as the composite tensile test.

After tensile test, fracture surfaces of the continuous fiber biobased composites were observed under a 4 K digital 3D microscope VHX-7000 from Keyence (Japan) equipped with a VHX-7100 fully integrated head and a VHX-E20 objective of $\times 20$ to $\times 100$ magnification range to evaluate the fracture morphology of the different constituents of the printed composites. All observations were recorded on 2880×2160 pixels images with $\times 50$ magnification under reflected light.

Internal structures of the continuous biobased composites were also observed by X-μCT after failure using a Desk-Tom 150 from RX Solutions (France) to investigate the internal damage mechanism that cannot be observed on surface observations such as internal cracking or delamination. The scanning step used an X-ray source with a voltage of 60 kV and a current intensity of 166 μA with a 1920×1536 pixels scintillation detector. The scanning consisted of 1440 radiographic images at 1.7 images/s with a voxel size of 8 μm. Once 2D images acquired, the 3D volume reconstruction is carried out on X-Act software version 2.0 from RX Solutions. For qualitative observations of the microstructure, a right rectangular prism of $17.62 \times 13.19 \times 5.50\,\text{mm}^3$ was selected around the fracture section of tensile test specimens and oriented with the specimen orientation to observe the whole width and thickness. X-μCT attributes different gray shades to different substances according to their densities, the denser the substance is, the lighter the color exhibits. An example is shown in Figure 7.

The X-μCT was also used to scan the untested samples to determine the quality of the material, the porosity rate, and the volume fraction of the fiber. The surface porosity rate (porosity appearing in black on Figure 7) was obtained by using quantitative tomographic images-based numeric analysis on MATLAB software on 1000 images. Mean value of surface porosity rates gave the global porosity rate of the sample and standard deviation (STD) gave an indication of the porosity distribution along the deposition. Porosities located inside the flax yarns are not included due to the difficulty of its evaluation. Indeed, the distances between fibers, where this type of porosity lies, are too small regarding the resolution of the tomography device, leading to blurry pixels whose composition, namely void or fibers, cannot be determined. The apparent volume fraction of the fiber was used for mechanical modelling as this apparent volume fraction represents the reinforcement included in the yarn outer perimeter, meaning that both elementary flax fibers and in-yarn porosity are considered during mechanical evaluation. This apparent volume fraction was determined from the apparent area, circled in red as depicted on Figure 7, using Image J software by mean of five image analysis for statistical analysis.

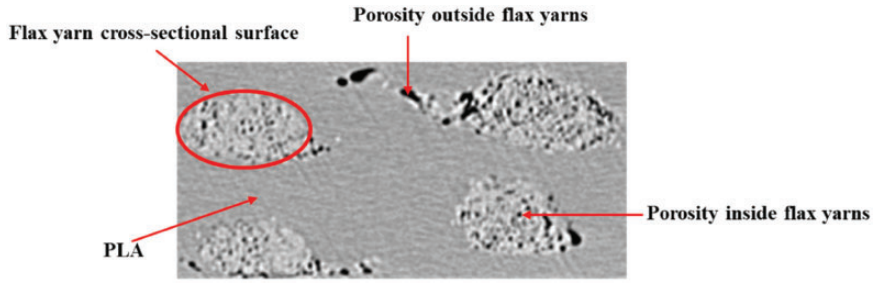

Figure 7. Example of the different constituents of a composite material acquired in X-μCT.

Results and discussion

Tensile properties of the AM continuous composites flax/PLA

Estimation and measurement of the mechanical properties of the 0°-oriented continuous composite. A first step consisted in measuring the properties of the different constituents, taken separately, and the properties of a 0°-oriented continuous fiber composite to compare their respective mechanical behaviors. Representative examples of tensile strain-stress curves of the flax yarn, the PLA 0° AM specimen, and the flax/PLA 0° AM specimen are compared in Figure 8. All the curves present a pseudo-brittle behavior. The flax yarn shows the highest tensile strength and stiffness, while the PLA 0° AM specimen curve shows the weakest tensile strength and stiffness, but the highest elongation at break. The continuous fiber composite curve exhibits an intermediate behavior.

One should remark that at the early stage of the tensile test, PLA, and PLA/flax specimens both show linear stress-strain relation. The flax yarn shows a nonlinear stress-strain relation with a tendency of being stiffer with the increase of the tensile load, which corresponds to the stage where the twisted flax fibers of the yarn (shown in Figure 9) arrange themselves with the loading axis during the tensile loading (Moothoo et al., 2014). Then, a linear elastic region is observed where the slope is used to determine the tensile modulus of the flax yarn, until it reaches a nonlinear stage just before the fracture point, potentially due to the damage of the flax fibers or interfaces and rearrangements occurring within the flax yarn (Moothoo et al., 2014).

After being reinforced with the continuous flax fiber along 0°, the PLA/flax composite has significantly higher UTS and Young's modulus than the PLA specimen, while the composite elongation at break approximately equals that of the flax fiber yarn (see Table 4). For the composite reinforced with continuous yarns oriented along tensile direction, the failure of the composite depends on the failure of the component having the lowest breaking strain, namely the flax yarn in this case, which leads to similar elongation at break for the composite and the yarns. Inside the composite during tensile test, the continuous flax yarn and the polymer went through the same strain until the fracture of the flax yarns arrived.

Comparing the pure PLA with the PLA/flax composite under the same printing conditions (see Table 4), reinforcement of the continuous flax fiber increased the UTS and the Young's modulus by 2.6 and 3.8 times, respectively. These results are consistent with those obtained by Kuschmitz et al. (2021). After reinforcement, the composite has approximately the same elongation at break as the flax fiber yarn, which is inferior to the pure PLA. In this case, the estimation of tensile strength at

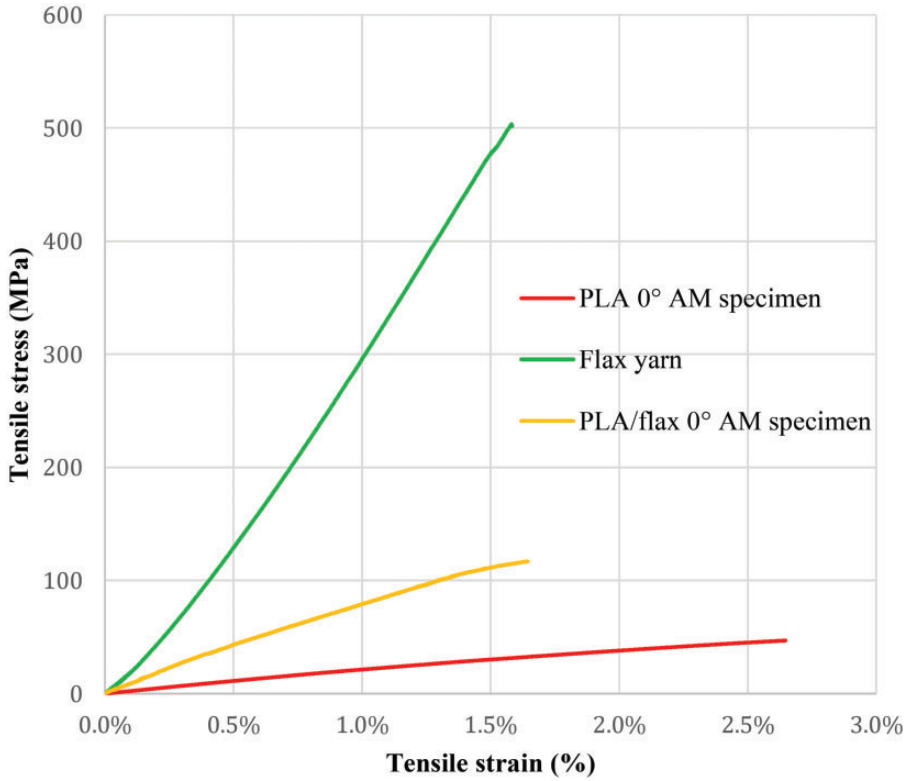

Figure 8. Comparison of representative tensile curves of the PLA/flax composite, the pure PLA, and the flax yarns specimens.

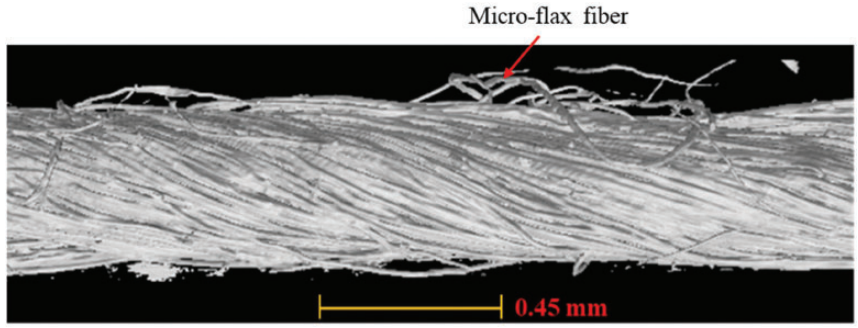

Figure 9. 3D tomographic image of the flax yarn structure.

fracture and Young's modulus of the composite had been done according to the rule of mixtures, reading:

$$\sigma_{cu} = \varphi_f \sigma_{fu} + \varphi_m (\sigma_m)_{\varepsilon_{fu}} \tag{2}$$

$$E_c = \varphi_f E_f + \varphi_m E_m \tag{3}$$

with σ_{cu} and σ_{fu} the UTS of the composite and the flax yarn, respectively; $(\sigma_m)_{\varepsilon_{fu}}$ the tensile stress of the polymer at the elongation at break of the yarn; φ_f and φ_m the volume fractions of the fiber and of the matrix, respectively; and E_c, E_f and E_m the Young's moduli of the composite, the fiber yarn and the matrix, respectively.

One must remark that the rule of mixture commonly uses the Young's modulus of the flax fiber, while E_f in (3) is the Young's modulus of the flax yarn, which, in this situation, is regarded as a homogeneous phase of the composite. This hypothesis is consistent with the scale of the specimen and the disposition of the fibers in the composite, which make it behaves as the flax yarn during its characterization (see Section 'Material characterization'). Indeed, flax fiber length is reported in the literature to range from 4 to 77 mm, with a mean value of 33 mm (Baley, 2002). The gauge length for tensile test of the flax yarn and the composite specimen was set as 140 mm, which means there was no elementary fiber clamped to both tensile jaws. Thus, the tensile properties of the neat flax yarn and of the flax yarn inside the composite specimen both consider the mechanical behavior of the flax fiber bundle and their fiber/fiber interfaces (Moothoo et al., 2014). Therefore, the use of Young's modulus of the flax yarn in the estimation is more representative of the real experiment and it could reduce the misestimation of the model. Summary of the data are displayed in Table 4.

The porosity rate and the apparent fiber volume fraction of the AM composite specimens were estimated as 8% (STD $\approx$ 0.08%) and 21% (STD $\approx$ 0.35%), respectively, leading to a polymer volume fraction $\varphi_m = 71\%$. Then, equations (2) and (3) lead to a Young's modulus of 127 MPa and an UTS of 9.0 GPa (see Table 4), which is close to the experimental Young's modulus and the UTS, reading 123 ± 5 MPa and 9.2 ± 0.6 GPa respectively.

The correspondence of the experimental and theoretical results indicates that the tensile behavior of the additively manufactured composite follows the rule of mixtures, and that the internal defects of the composite did not have a significant impact on the tensile properties of the 0° AM PLA/flax composite. Still, this result remains an indication, as it relies on imprecise volume fraction measurements, as can be seen in Figure 7. We also observe that the flax/PLA composite has a slightly higher tensile elongation at break than the flax yarns (Figure 8), which indicates that the porosities inside the polymer did not have much impact on the tensile behavior of the composite and that the printing quality, and specifically the fiber/matrix bonding, is good. This is consistent with the UTS being more interesting than that of Kuschmitz et al. (2021) while the fiber content of the material in this study is slightly lower than theirs 21% compared to 24%.

Comparison of tensile properties of the 0°, 45° and 90° AM PLA/flax composites. Figure 10 depicts the comparison of the tensile stress-strain curves of the 0°, 45° and 90° AM PLA/flax composites.

Table 4. Tensile properties of the flax yarn, PLA 0°-oriented AM specimen, and 0°-oriented AM composite specimen.

Material	Flax yarn	PLA 0°-oriented AM	0°-oriented AM composite	Estimated properties of composites
Young's modulus E (GPa)	34.8 ± 2.5	2.4 ± 0.1	9.2 ± 0.6	9
Ultimate tensile strength σ_u (Mpa)	492 ± 30	48 ± 3	123 ± 5	127
Elongation at break ε_u	$1.63\% \pm 0.11\%$	$2.62\% \pm 0.16\%$	$1.69\% \pm 0.08\%$	/

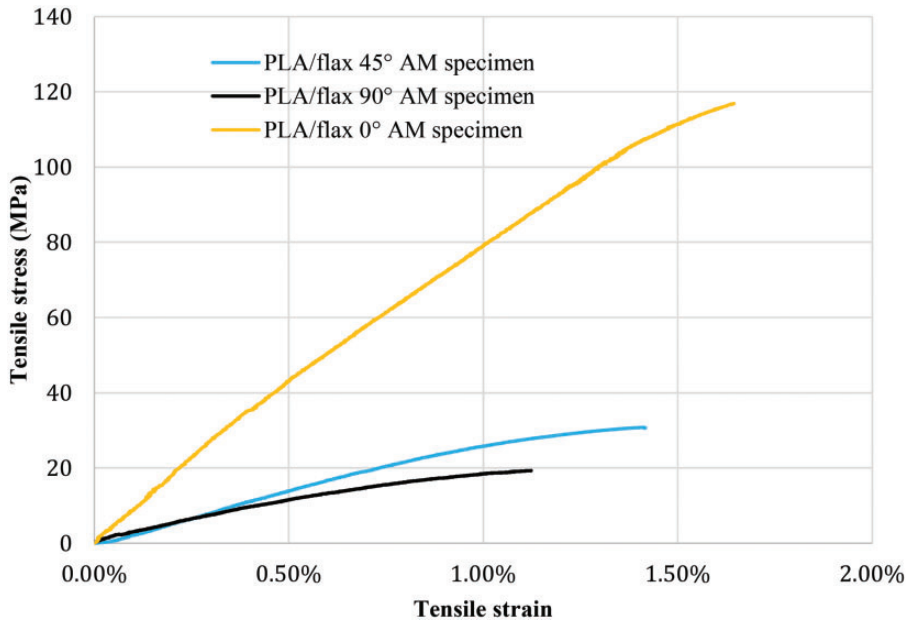

Figure 10. Representative tensile stress-strain curves of the PLA/flax composite AM specimens with 0°, 45° and 90° yarn orientations.

All the curves show a pseudo-brittle behavior. As expected, the 0° composite has the stiffest tensile curve with the highest tensile strength and elongation at break while the 90° one presented the flattest tensile curve with the lowest tensile strength and elongation at break. The tensile curve of the 45° composite shows the intermediate tensile strength and elongation at break, and the curve locates between the curves of the 0° and the 90° composites but close to the 90° one.

One can remark that for the 0° composites, there is an elastic linear slope at the early stage until a stress of ~35 MPa and a strain of ~0.26%, followed by a slight decline of stiffness that could be due to an early damage or plastic strain in the polymer. Indeed, Figure 8 shows that the nonlinear stage of the pure PLA reaches around 0.6% in strain and 15 MPa in stress. Both the 45° and 90° composite curves also exhibit a linear stress-strain relation at the early stage and turn nonlinear for the rest of the curves until the fracture is reached.

The measured tensile properties of the AM composites for different yarn orientations are presented in Table 5. An increase in yarn orientation leads to a sharp decrease in tensile properties from 0° to 45°, followed by a slight decrease from 45° to 90°. It is a classical result for unidirectional composite material obtained with classical processes or AM as can be seen in the literature (González-Estrada et al., 2018; Le Duigou et al., 2019; Mohammadizadeh and Fidan, 2021). Indeed, when the composite is loaded in the main direction of the yarn (0° direction), the load is mainly supported by the yarns which act as the main reinforcing component. When the yarns are not oriented in the loading direction, their contribution to the mechanical behavior is less significant.

For the 90° configuration, a drop in Young's modulus and UTS is observed of the order of 74% and 85% respectively compared to the 0° configuration (see Table 5). At this configuration, the contribution of the polymer to the overall behavior of the composite is predominant. This is confirmed by the measured Young's modulus (2.4 MPa), which is close to the modulus of the printed

Table 5. Tensile properties of the AM continuous flax/PLA specimens with different yarn orientations.

Fiber orientation compared to tensile direction (°)	0	45	90
Young's modulus E (GPa)	9.2 ± 0.6	3.0 ± 0.4	2.4 ± 0.4
Ultimate tensile strength σ_u (MPa)	123 ± 5	28 ± 2	20 ± 2
Ultimate tensile strain ε_u	$1.69\% \pm 0.08\%$	$1.21\% \pm 0.2\%$	$1.14\% \pm 0.1\%$

Table 6. Tensile properties of the AM PLA specimens with different AM orientations (Casavola et al., 2016).

AM orientation compared to tensile direction (°)	0	45	90
Young's modulus E (GPa)	3.12 ± 0.03	2.86 ± 0.02	2.77 ± 0.32
Ultimate tensile strength σ_u (MPa)	50.23 ± 0.77	40.68 ± 0.75	22.49 ± 0.75
Ultimate tensile strain ε_u	2.1%	1.8%	1.0%

polymer specimen (see Tables 4 and 5). Casavola et al. (2016) studied the influence of AM orientation of pure PLA on the tensile properties. The summary of their results is shown in Table 6. The tensile properties of additively manufactured PLA specimens decrease with the increase of AM orientation. The decrease of the Young's modulus is slight compared to the decrease of the tensile strength and of the elongation at break as the Young's modulus hardly depends on the inter-raster properties, while the UTS depends on surface defects, namely micro-cracks, in the composite, and particularly on the inter-raster bonding that is solicited for 90° AM PLA specimen. Comparing the pure PLA specimens (Casavola et al., 2016) with the composite specimens (see Table 5), the PLA/flax 0° AM composite has significantly higher UTS and Young's modulus than the 0° AM PLA without reinforcement. Similar results were found in 3.1.1 section (see Table 4). However, the reinforcement with 45° and 90° fiber orientation did not enhance the tensile properties of the materials. Similar results were found by Le Duigou et al. (2019) with the 90° reinforced PLA/flax AM composite that showed negligible tensile enhancement compared to the 0° one. The longitudinal tensile load is predominantly taken by the fibers at a 0° orientation as they play the role of main bear-loading component (Mohammadizadeh and Fidan, 2021). On the contrary, the UTS and elongation at break seems inferior for composite specimens than for pure PLA, with similar Young's modulus (see Tables 5 and 6), meaning that early damage could occur with the presence of fibers unaligned with the tensile stress direction. This behavior could mean that fiber/polymer bonding has inferior mechanical properties than inter-raster adhesion. With 45° and 90° fiber orientations and 45° and 90° polymer raster depositions, the composite fracture was mainly driven by the polymer inter-raster adhesion and/or the fiber/polymer interface bonding. As inter-raster adhesion and fiber/polymer interface bonding have inferior tensile properties compared to intra-yarn cohesion ones, those 45° and 90°-oriented composites prematurely break compared to the 0° AM composite where the continuous yarn drives the composite's tensile properties. Therefore, the continuous flax/PLA AM composites show a more pronounced anisotropy than pure PLA AM materials both regarding the variation amplitude in tensile properties and the fast decrease in tensile properties with the orientation deviation from the 0° orientation.

For the 90° AM flax/PLA composite, the Young's modulus can be estimated by using Reuss model (shown in equations 4 and 5). With φ_f' and φ_m' the flax yarn and PLA matrix volume fracture without considering any porosity inside the specimen, E_c' the composite Young's modulus

without considering any porosity inside the specimen, and E_c the composite Young's modulus when the porosity rate φ_p outside of the flax yarn is counted.

$$\frac{1}{E_c'} = \frac{\varphi_f}{E_f} + \frac{\varphi_m'}{E_m} \tag{4}$$

$$E_c = E_c' \cdot (1 - \varphi_p) \tag{5}$$

The estimated Young's modulus of the 90° composite was calculated as 2.8 GPa which corresponds to the experimental result of 2.4 ± 0.4 GPa (see Table 5).

Fracture and damage morphology analysis

Microscopic image analysis. Following the mechanical characterization of the specimens, fracture zones were observed to assess the failure mode and damage mechanism. Figure 11 shows pictures of the fracture of the composite specimens after tensile tests as observed at the naked eye. The specimens show brittle fracture which is consistent to the previous analysis of their tensile curves.

The 0° specimens are the only ones where fiber yarn failure is observed, as they are oriented along the loading direction. This indicates that the flax fibers have taken important load during the tensile test. The rupture section is slightly tortuous and contains broken fiber pull-out, which is different from the clean fracture surface of 0° printed PLA specimens (Vanaei et al., 2021). An almost straight fracture is observed and is assumed due to a rupture occurring at different locations in

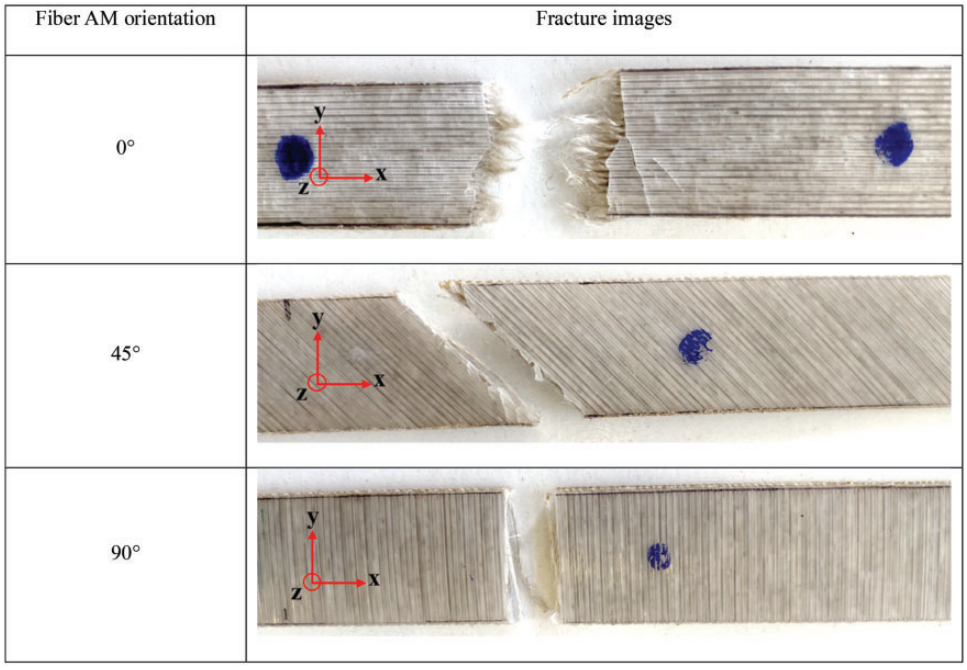

Figure 11. Photographs of fracture areas of flax/PLA specimens with fiber orientations of 0°, 45° and 90°.

the x-axis from both sides of the specimen before propagating and merging after a deviation as this trajectory requires less energy for its propagation.

The 45° and 90° printed composites show clean fracture surfaces as the 45° and 90° printed PLA specimens in the study of (Khosravani et al., 2022a), the exposed yarns remain plain, and the fracture directions are parallel to the printing directions and thus the fiber orientations, which could indicate that the failure could be due to the polymer inter-raster delamination or polymer/fiber interface debonding. The fracture facies of the 45° specimens indicate a failure in shear mode. The polymer inter-raster delamination is a specific fracture phenomenon for AM materials, especially when the AM orientation deviates from the tensile direction. This specificity is due to the manufacturing mode consisting of depositing raster after raster and where the coalescence between two adjacent rasters defines the quality of the material cohesion, which influences its behavior when it is mechanically loaded outside its printing axis. Similar results was observed by Ginoux et al. (2023) with 45° and 90° printed PETG specimens showing a clean fracture mode parallel to their AM orientations. From the study of Le Duigou et al. (2019), the 90° AM PLA/flax composite showed a fracture trajectory parallel to the yarn orientation without breakage of the flax yarn, while the 0° one had a more tortuous fracture with ruptured flax yarns. Thus, the effect of the inter-raster on the mechanical behavior is valid both on printed composite materials but also on printed polymer materials since the structure of the latter after printing is assimilated to that of composites, the rasters being assimilated to threads.

A deeper look on the fracture zones is necessary to verify at the microscopic scale the hypothesis drawn at the macroscopic scale. For this, the fracture zones of the same samples were observed under digital 3D microscope. Figure 12 illustrates the 3D microscopic images of the fracture surfaces of the differently oriented AM composites.

The 0° AM composite fracture region shows the rupture of the flax yarns and the polymer rasters perpendicular to the printing direction. The fracture region of the 45° AM composite shows the intra-raster polymer rupture and no evident flax yarn breakage and the 90° AM composite shows the inter-raster polymer rupture and the flax yarn stays complete without evident damage. For the three specimens, there is no evident polymer residue remaining on the flax fibers or inside the pulled-out yarns, which indicates the weak polymer impregnation effect specifically inside the yarns. The weak impregnation issue of the biobased composites is due to its nature and structure of the yarns made up of non-continuous fibers, and therefore requiring treatment and/or twisting during its spinning (A. Mohanty et al., 2000). As the used flax yarn in this study has a highly twisted structure of 150 tpm (see Table 1 and Figure 9), it could bring difficulties for the polymer to impregnate the yarn due to its high viscosity in its molten state. Interface bonding strength between fiber and matrix also participates in maintaining high mechanical properties of composite materials by giving higher stress transfer throughout the interface of the composite (Kabir et al., 2012). However, the lack of impregnation of the yarn contributes to reducing the total surface area of this fiber/polymer interface.

Tomographic images analysis. μ-XCT scans were performed to observe the internal structure of the fracture regions to assess the internal damages. Examples of tomographic images are displayed in Figure 13 in the transverse cut and in plane cut.

For the 0° AM composite, no inter-layer delamination of the specimen is observed in the planes orthogonal to the fiber orientation as illustrated by the Figure 13(a), which presents a section captured near the fracture region, contrary to what was observed by Heitkamp et al. (2023). This demonstrates good coalescence between the composite layers and therefore its good quality and the benefit effect of the used specimen preparation method. Certain fiber yarns are missing in this

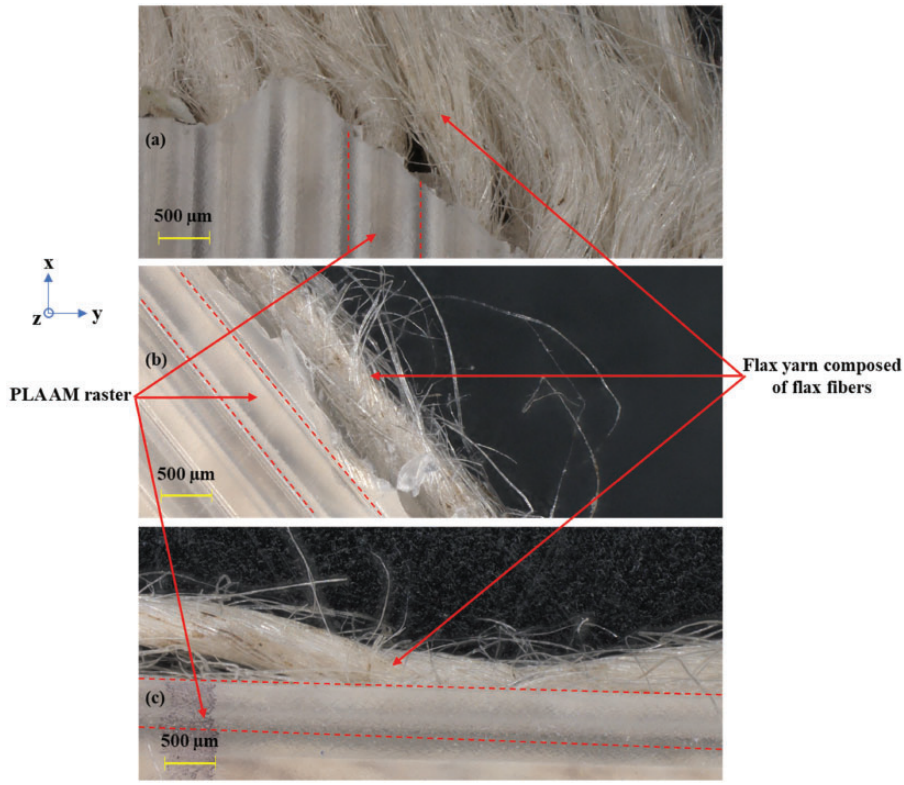

Figure 12. Digital 3D microscopic images of fracture regions of the composites: (a) 0° AM, (b) 45° AM and (c) 90° AM.

section and are attributed to the fiber pull-out as can be seen on the Figure 13(b) and (c). Fiber yarns pull-out is a common phenomenon found in natural fiber composite studies, which is due to the weaker fiber/matrix interface bonding strength compared to the shear forces at the interface during tensile test (Sause, 2016). The weak fiber/matrix interface bonding is originally caused by the imperfect impregnation effect during AM due to the highly twisted fiber yarn structure (Cheng et al., 2021; A. K. Mohanty et al., 2001). As the polymer does not fully impregnate the biobased yarns, pull-out of the yarn during failure is observed (Figure 13(a)) as the fiber/matrix interface is essentially located on the outer contour of the yarns. In comparison with composites reinforced with carbon or glass fibers, pull-out of individual fibers can be locally observed rather than bundles of fibers (Matsuzaki et al., 2016).

Polymer cracks across the thickness of the specimen – oriented in the z axis – can also be observed in the Figure 13(a). The crack circumvents the yarns – either left or right – each time, which indicates that in this zone the interface has yielded. In addition, the flax yarns failure can affect the damage and crack of the polymer matrix nearby because the continuous flax yarn-reinforced PLA composites are considered as materials with high stiffness. During the fiber failure, the released energy is often more than necessary to just crack the fiber. This might cause fiber/matrix debonding or damage propagation in the surrounding matrix immediately after the fiber break, which propagates the matrix damage until the neighboring fiber is reached

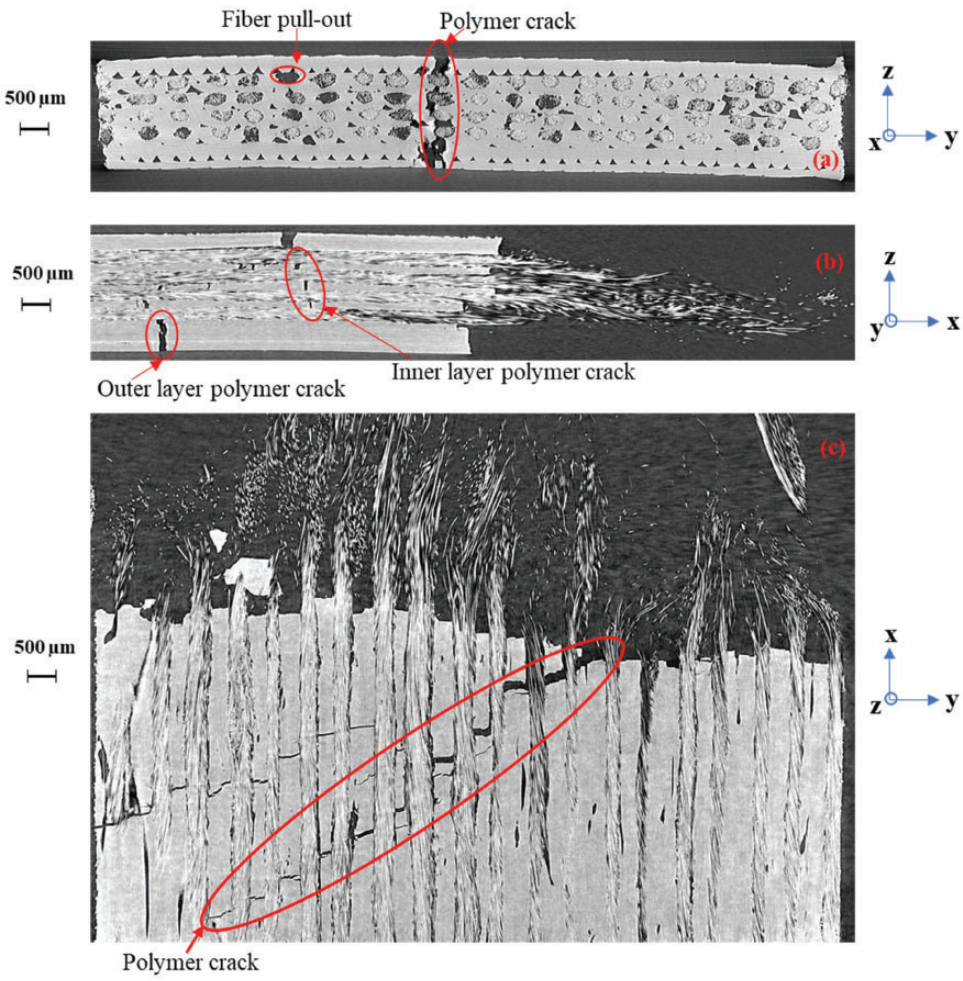

Figure 13. Tomographic images of the fracture region of the 0° AM flax/PLA composite observed from (a) x, (b) y and (c) z axis direction. Blue arrows represent the axes with (xy) the layer plane and (xz) the plane orthogonal to the deposition direction.

(Pupurs et al., 2013). This is what causes several zones of polymer cracks near the fracture region of the specimen as it can be seen in Figure 13(b) and (c). This polymer brittle cracks are present in the thickness and the width of the specimen (oriented in the z axis and y axis) as illustrated in the three images (see Figure 13). This illustrates a 3D damage mechanism that presented an irregular zigzag-like shape (see circle in Figure 13(c)) that can be attributed to the inhomogeneous mechanical resistance of the polymer and/or the role of the porosity (Majumdar and Hunston, 2001).

Figures 14 and 15 illustrate the fracture of AM specimen printed at 45° and 90° in raster orientation as observed by µ-XCT scans. The inclined fracture section of the 45° specimens indicates a failure in shear mode. For both 45° and 90° AM composites, the failures are clean with no evident matrix damage outside of the failure region. The black areas observed in the images are porosities and not damage, the majority of which is located at the interfaces of the exterior folds (see Figures 14 and 15).

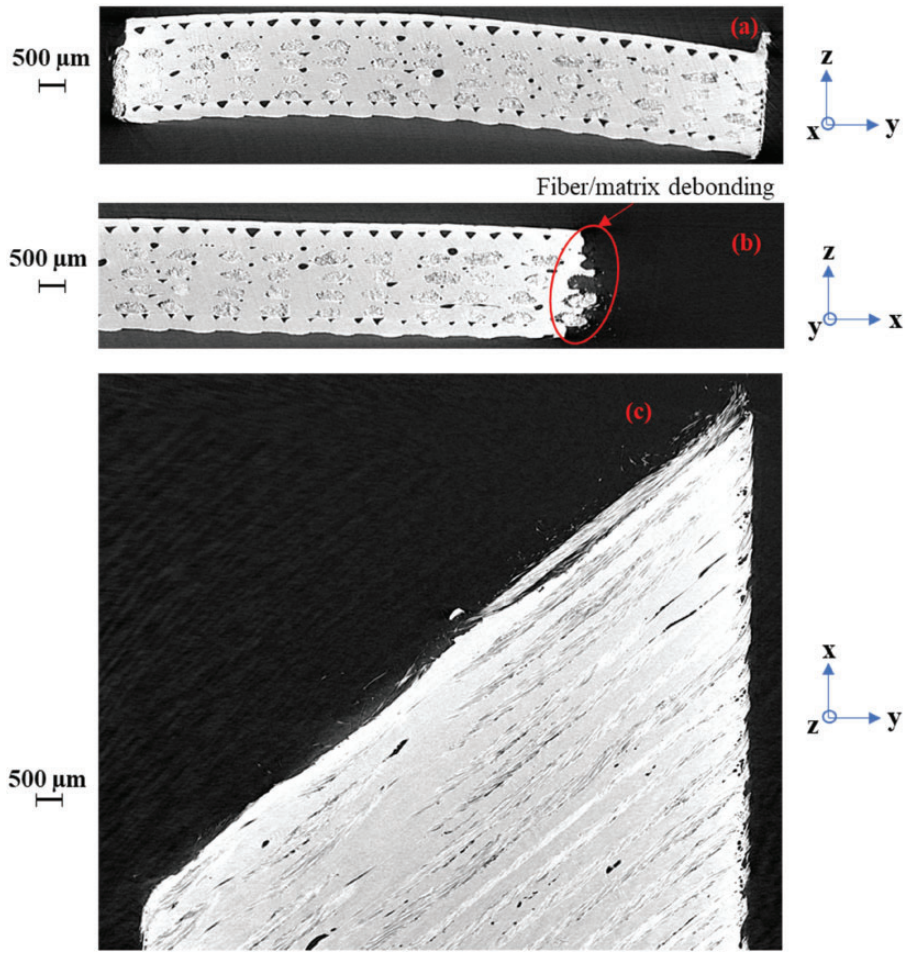

Figure 14. Tomographic images of the fracture region of the 45° AM flax/PLA composite observed from (a) x, (b) y and (c) z axis direction.

One should note that failure with open cavities of the shape of the yarn is observed, which shows a loosening of the yarn out of its location (see Figures 14(b) and 15(b)). This can be attributed to fiber/matrix debonding due to the weaker fiber/matrix adhesion compared to the polymer/polymer adhesion, namely inter-raster interface. This weaker fiber/matrix adhesion is in accordance with previously discussed results that are obtained with the observation on digital 3D microscope (Figure 12) where no polymer residue remains on fibers.

Unlike the 0° AM composite where the tensile load was predominantly taken by the longitudinal fibers, the UTS for the 45° and 90° AM composites mainly depends on the fiber/polymer interface bonding strength. As less force is applied on the fibers, no excessive energy is released that could have caused adjacent polymer cracking as detailed by Pupurs (2009) (see Figures 13 to 15). Consequently, unalignment of the thread with the tensile direction leads to sudden fracture and explains the decrease in mechanical properties from 0° to 90° in orientation regarding Young's modulus, UTS and elongation at break (see Figure 10). A fracture happening at the weaker

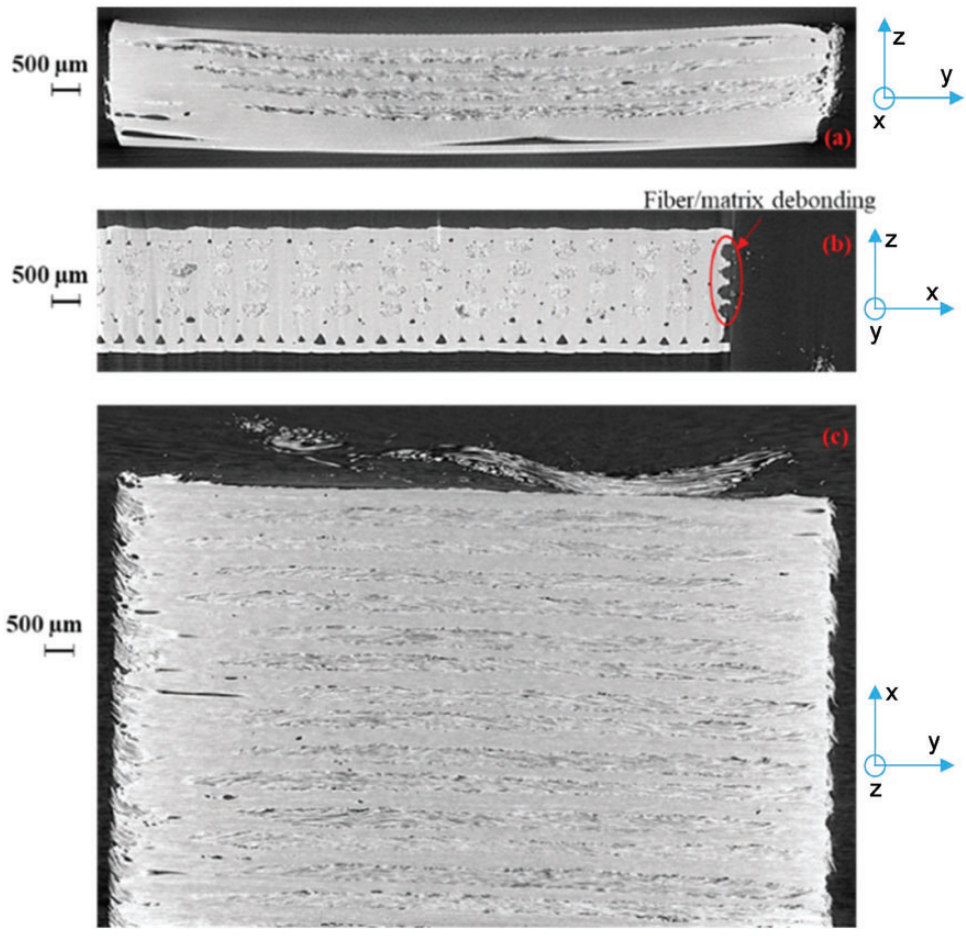

Figure 15. Tomographic images of the fracture region of the 90° AM flax/PLA composite observed from (a) x, (b) y and (c) z axis direction.

fiber/polymer interface rather than at the raster/raster interface also agrees with lower mechanical properties at 45° and 90° as discussed in section 'Comparison of tensile properties of the 0°, 45° and 90° AM PLA/flax composites' since the addition of fibers act as a fracture initiator in the transverse direction along the fiber/polymer interface.

Conclusion and perspectives

The in-nozzle impregnation AM of continuous flax fiber-reinforced composites have a low environmental impact and good mechanical properties. The tensile tests showed that with longitudinal reinforcement of the continuous flax fiber yarn, the elastic modulus and tensile resistance of the flax/PLA composite were evidently improved compared to the unreinforced additively manufactured PLA. The good quality of the printed material and the use of adapted specimen preparation method led to high UTS and good consistency between the estimated properties and the experimental ones.

The failure of the specimens printed at different orientations was brittle and showed classic facies for composites. No inter-layer delamination of the material was observed due to good coalescence between the composite layers and the adapted specimen preparation method that avoid creating defected areas for damage initiation.

For the 0° AM composite, the flax fibers took most of the tensile load, which resulted in the fiber damage and fiber rupture. The failure occurred in the form of fiber yarns pull-out releasing energy which causes damage to propagate into the matrix in the immediate vicinity of the failure. In 3D damage mechanism that presented an irregular zigzag-like shape that can be attributed to the inhomogeneous mechanical resistance of the polymer and/or the role of the porosity. This also produced a fiber/matrix debonding in the form of cracks that circumvent the yarns either left or right side. The fiber/matrix debonding is caused by the imperfect impregnation of the polymer in the flax yarn due to the nature of the yarn itself, its structure, and the fact that it has often highly twisted fiber bundle structure.

Fiber/matrix debonding is the predominant mechanism governing the failure behavior of the 45° and 90° printed specimens, where the composite failures are clean with no evident matrix damage outside of the failure region. An orientation of the yarns during AM different to the loading direction results in a lower breaking stress and energy than for materials printed at 0°. Thus, regardless of the printing orientation and despite the improvements brought by the specimen preparation protocol and the good printing quality, the fiber/matrix bonding has proven to be an important mechanism for the failure of the composite since no polymer residue was observed on the pulled-out or broken fibers and yarns.

This work highlights the main damage mechanisms in continuous reinforced biobased composites regarding the different orientations of the reinforcement and allowed drawing future recommendations of studies to improve their mechanical performance. In this way, improving the fiber/matrix interface, that was demonstrated as the main and critical damage mechanism, would increase the breaking performance of the composite reinforced with continuous flax fibers. Future studies should focus on an enhanced compatibilization between vegetal fibers and matrix by chemical treatment or by optimizing the AM impregnation in the nozzle.

Acknowledgements

This project is included in the MATUR Chair, co-financed by the Grand Est region (France), the Ardenne Metropole. Platinium 3D (France) is thanked for providing the 3D microscopic images.

Declaration of conflicting interests

The author(s) declared no potential conflicts of interest with respect to the research, authorship, and/or publication of this article.

Funding

The author(s) received no financial support for the research, authorship, and/or publication of this article.

ORCID iD

Samir Allaoui https://orcid.org/0000-0001-9673-1016

References

Bahrami M, Abenojar J and Martínez M Á (2020) Recent progress in hybrid biocomposites: Mechanical properties, water absorption, and flame retardancy. *Materials* 13(22): 5145.

Baley C (2002) Analysis of the flax fibres tensile behaviour and analysis of the tensile stiffness increase. *Composites Part A: Applied Science and Manufacturing* 33(7): 939–948.
Balla V K, Kate K H, Satyavolu J, et al. (2019) Additive manufacturing of natural fiber reinforced polymer composites: Processing and prospects. *Composites Part B: Engineering* 174: 106956.
Bisanda E T N and Ansell M P (1992) Properties of sisal-CNSL composites. *Journal of Materials Science* 27(6): 1690–1700.
Casavola C, Cazzato A, Moramarco V, et al. (2016) Orthotropic mechanical properties of fused deposition modelling parts described by classical laminate theory. *Materials & Design* 90: 453–458.
Chen K, Yu L, Cui Y, et al. (2021) Optimization of printing parameters of 3D-printed continuous glass fiber reinforced polylactic acid composites. *Thin-Walled Structures* 164: 107717.
Cheng P, Wang K, Chen X, et al. (2021) Interfacial and mechanical properties of continuous ramie fiber reinforced biocomposites fabricated by in-situ impregnated 3D printing. *Industrial Crops and Products* 170: 113760.
Dhakal H, Zhang Z and Richardson M (2007) Effect of water absorption on the mechanical properties of hemp fibre reinforced unsaturated polyester composites. *Composites Science and Technology* 67(7–8): 1674–1683.
Dutra T A, Ferreira R T L, Resende H B, et al. (2020) Expanding puck and Schürmann inter fiber fracture criterion for fiber reinforced thermoplastic 3D-printed composite materials. *Materials* 13(7): 1653.
Ginoux G, Dony P, Vroman I, et al. (2021) Improving thermomechanical properties of fused filament fabrication printed parts by using nanocomposites. *Composites Part B: Engineering* 224: 109227.
Ginoux G, Paux J and Allaoui S (2023) New preparation method of microstructurally and mechanically standardized PETG specimens by material extrusion additive manufacturing and machining. *Additive Manufacturing* 66: 103471.
González-Estrada O A, Pertuz A and Quiroga Mendez J E (2018) Evaluation of tensile properties and damage of continuous fibre reinforced 3D-Printed parts. *Key Engineering Materials* 774: 161–166.
Heitkamp T, Girnth S, Kuschmitz S, et al. (2023) Experimental and numerical investigation of the mechanical properties of 3D-printed hybrid and non-hybrid composites. *Polymers* 15(5): 1164.
Isobe T, Tanaka T, Nomura T, et al. (2018) Comparison of strength of 3D printing objects using short fiber and continuous long fiber. *IOP Conference Series: Materials Science and Engineering* 406: 012042.
Kabir M M, Wang H, Lau K T, et al. (2012) Chemical treatments on plant-based natural fibre reinforced polymer composites: an overview. *Composites Part B: Engineering* 43(7): 2883–2892.
Kasmi S, Ginoux G, Allaoui S, et al. (2021) Investigation of 3D printing strategy on the mechanical performance of coextruded continuous carbon fiber reinforced PETG. *Journal of Applied Polymer Science* 138(37): 50955.
Khosravani M R, Berto F, Ayatollahi M R, et al. (2022a) Characterization of 3D-printed PLA parts with different raster orientations and printing speeds. *Scientific Reports* 12(1): 1016.
Khosravani M R, Frohn-Sörensen P, Reuter J, et al. (2022b) Fracture studies of 3D-printed continuous glass fiber reinforced composites. *Theoretical and Applied Fracture Mechanics* 119: 103317.
Kuschmitz S, Schirp A, Busse J, et al. (2021) Development and processing of continuous flax and carbon fiber-reinforced thermoplastic composites by a modified material extrusion process. *Materials* 14(9): 2332.
Le Duigou A, Barbé A, Guillou E, et al. (2019) 3D printing of continuous flax fibre reinforced biocomposites for structural applications. *Materials & Design* 180: 107884.
Liu T, Butaud P, Placet V, et al. (2021) Damping behavior of plant fiber composites: A review. *Composite Structures* 275: 114392.
Majumdar B S and Hunston D (2001) Continuous parallel fiber composites: Fracture. In: Buschow KHJ, Cahn RW, Flemings MC, et al. (eds) *Encyclopedia of Materials: Science and Technology*. Amsterdam: Elsevier, pp. 1618–1628.
Matsuzaki R, Ueda M, Namiki M, et al. (2016) Three-dimensional printing of continuous-fiber composites by in-nozzle impregnation. *Scientific Reports* 6(1): 23058.
Mohammadizadeh M and Fidan I (2021) Tensile performance of 3D-printed continuous fiber-reinforced nylon composites. *Journal of Manufacturing and Materials Processing* 5(3): 68.

Mohanty A K, Misra M and Drzal L T (2001) Surface modifications of natural fibers and performance of the resulting biocomposites: An overview. *Composite Interfaces* 8(5): 313–343.

Mohanty A, Misra M and Hinrichsen G (2000) Biofibres, biodegradable polymers and biocomposites: An overview. *Macromolecular Materials and Engineering* 276(1): 1–24.

Moothoo J, Allaoui S, Ouagne P, et al. (2014) A study of the tensile behaviour of flax tows and their potential for composite processing. *Materials & Design* 55: 764–772.

Pereira T, Kennedy J V and Potgieter J (2019) A comparison of traditional manufacturing vs additive manufacturing, the best method for the job. *Procedia Manufacturing* 30: 11–18.

Pupurs A (2009) *Fracture mechanics analysis of damage initiation and evolution in fiber reinforced composites*. Luleå Tekniska Universitet, Licentiate thesis.

Pupurs A, Krasnikovs A and Varna J (2013) Energy release rate based fiber/matrix debond growth in fatigue. Part II: Debond growth analysis using Paris law. *Mechanics of Advanced Materials and Structures* 20(4): 288–296.

Ramamoorthy S K, Skrifvars M and Persson A (2015) A review of natural fibers used in biocomposites: Plant, animal and regenerated cellulose fibers. *Polymer Reviews* 55(1): 107–162.

Rao Y, Wei N, Yao S, et al. (2021) A process-structure-performance modeling for thermoplastic polymers via material extrusion additive manufacturing. *Additive Manufacturing* 39: 101857.

Rocher J-E, Allaoui S, Hivet G, et al. (2015) Experimental characterization and modeling of GF/PP commingled yarns tensile behavior. *Journal of Composite Materials* 49(21): 2609–2624.

Saidane E H, Arnold G, Louis P, et al. (2022) 3D printed continuous glass fibre-reinforced polyamide composites: Fabrication and mechanical characterisation. *Journal of Reinforced Plastics and Composites* 41(7–8): 284–295.

Sause M (2016) Failure of fiber-reinforced composites. In: *In Situ Monitoring of Fiber-Reinforced Composites. Springer Series in Materials Science*, vol 242. Cham: Springer. https://doi.org/10.1007/978-3-319-30954-5_2.

Sugiyama K, Matsuzaki R, Malakhov A V, et al. (2020) 3D printing of optimized composites with variable fiber volume fraction and stiffness using continuous fiber. *Composites Science and Technology* 186: 107905.

Terekhina S, Egorov S, Tarasova T, et al. (2022) In-nozzle impregnation of continuous textile flax fiber/polyamide 6 composite during FFF process. *Composites Part A: Applied Science and Manufacturing* 153: 106725.

van de Werken N, Tekinalp H, Khanbolouki P, et al. (2020) Additively manufactured carbon fiber-reinforced composites: State of the art and perspective. *Additive Manufacturing* 31: 100962.

Vanaei H R, Shirinbayan M, Vanaei S, et al. (2021) Multi-scale damage analysis and fatigue behavior of PLA manufactured by fused deposition modeling (FDM). *Rapid Prototyping Journal* 27(2): 371–378.

Zhang H and Sun W (2022) Mechanical properties and failure behavior of 3D printed thermoplastic composites using continuous basalt fiber under high-volume fraction. *Defence Technology* 27: 237–250.

Zhang J, Zhou Z, Zhang F, et al. (2020) Performance of 3D-printed continuous-carbon-fiber-reinforced plastics with pressure. *Materials* 13(2): 471.